

# How hydraulic fracturing triggers fault slip by raising fluid pressure

Luyi W. Shen<sup>\*1,2</sup>, Douglas R. Schmitt<sup>3</sup>, and Ryan Schultz<sup>2</sup>

<sup>1</sup>Institute of Geophysical Research, Department of Physics, University of Alberta, Edmonton, AB, Canada

<sup>2</sup>Alberta Geological Survey, Alberta Energy Regulator, Edmonton, AB, Canada

<sup>3</sup>Department of Earth, Atmospheric and Planetary Science, Purdue University, West Lafayette IN, USA; formerly at Institute for Geophysical Research, Department of Physics, University of Alberta, Edmonton, AB, Canada

\*Contact: [luyi@ualberta.ca](mailto:luyi@ualberta.ca) (dated Mar 16, 2019)

## Summary

*Earthquakes induced during hydraulic fracturing operations have occurred in a number of locales, but the triggering mechanisms remain poorly understood. Here, we study the fault slip-tendencies of eleven earthquakes that are linked to hydraulic fracturing stimulations of an unconventional hydrocarbon reservoir in a historically aseismic area. We use a recently constructed quantitative model for in-situ stresses and pore pressures to show that the faults could not be stable at the natural high ambient pore pressures extant within the target Duvernay Formation. To retain stability, the fluid pressures acting on the fault must be diminished; but locally these could readily be increased above the critical value if a hydraulic connection exists between the fault and a propagating hydraulic fracture within which pressures in excess of the minimum compression exist. The critical pressures necessary to induce slip are estimated using a probabilistic model that incorporates uncertainties of stress and fault mechanical properties.*

The rapid adoption of horizontal multi-stage hydraulic fracturing has transformed the global upstream oil and gas industry in the last decade and may be important in the future design of engineered geothermal systems. Although Hydraulic Fracturing (HF) operations are often associated with microseismicity ( $M_w < 0$ ), the process by itself is insufficiently energetic to produce larger earthquakes. Correspondingly, in contrast to the significantly greater numbers of earthquakes associated with broader long-term fluid disposal (1), there are few instances where HF has been linked to felt earthquakes. In HF induced earthquakes, it is probable that small perturbations in stress or fluid pressures triggered incipiently unstable faults.

The dynamic behaviour of faults during slip is complex and controlled by rate-dependent friction coefficient (2) that also depends on temperature (3) and fluid conditions (4). Slip initiation, in contrast, is usually assumed to be governed by Coulomb's law of friction as regulated by the static-friction coefficient  $\mu$  (5) and the fluid pressure  $P_f$  on the slip plane, through the Terzaghi effective stress law for shear failure (6, 7). Accordingly, slip initiates when the ratio of the fault shear  $\tau$  to normal  $\sigma$  tractions ( $SNR$ , 8) overcomes fault friction  $\mu$ :

$$\mu < \frac{\tau - C}{\sigma - P_f} \equiv SNR \quad . \quad (1)$$

Often, cohesion  $C$  of the fault plane is assumed to be small and has been ignored;  $\mu$  is often taken to fall between 0.6 and 1.0, although it may be lower in clay-rich fault gouges. If the tectonic stress states that generate the resolved tractions  $\tau$  and  $\sigma$  remains unchanged, then slip along the fault may be triggered by increasing  $P_f$ , a concept that was first tested by injection of water to a producing oil reservoir at Rangeley, Colorado (7). This necessitates an adequate fluid pathway to the fault from the HF operation.

Alternatively, slip could also be initiated by locally raising  $\tau$  or lowering  $\sigma$  which might be accomplished by additional loading during creation and propping of the stimulated fractures. However, which of these is primarily responsible for inducing earthquakes remains a topic of debate.

Over the Western Canada Sedimentary Basin, only a small fraction of HF stimulations have been linked to induced earthquakes with  $M_w \geq 3$  (9). These HF induced earthquakes are geographically clustered, with no induced events detected from the nearby operations targeting the same geological units (10).

Clustering of the seismicity has been statistically related to high natural formation pore pressure  $P_P$  (11), local geological structure (12), or volumes of injected fluids (10). Statistical correlations, however, cannot explain the proximate lack of seismicity nor resolve the physical mechanisms. The lack of knowledge of these processes limits the mitigation responses of recurrences to 'traffic light protocols' during HF operations (13).

### ***Slip tendency of faults reveal by earthquake's focal mechanism solutions***

Here, we carry out stability analyses using high-quality Focal Mechanism (FM) solutions for 11 induced earthquakes (Fig. 1, Supplementary Table S1) linked to HF operations in the Duvernay Formation near Fox Creek, Alberta (14). These analyses rely on a recently developed quantitative model for the full Andersonian tectonic principal stress magnitudes for the greatest  $S_H$ , least  $S_h$  horizontal and the vertical  $S_V$  compressions, as well the  $S_H$  azimuth  $\phi$  (15, 16).  $P_p$ ,  $S_h$ ,  $S_V$ , and  $\phi$  (Supplementary Fig. S1) are directly obtained from numerous borehole measurements within the Duvernay Formation and then used to calculate a range of absolute  $S_H$  (17) from the distribution of stress ‘shape factors’ determined from FM inversions (18) (see supplementary material). The inversion algorithm further provides the three orthogonal principal stress directions that are consistent with both the observed strike-slip mechanisms and with the Andersonian hypothesis that one principal stress is vertical (Fig. 1b). When resolved onto the FM inferred fault planes (Supplementary Table S1), these stresses allow us to calculate  $SNR$  distributions in order to carry out sensitivity tests on the factors affecting slip initiation with Eqn. 1.

Two adjacent HF-induced earthquakes ( $M_w$  3.6, Jan 23, 2015;  $M_w$  4.1, Jan 12, 2016) are selected in part because of the availability of additional active-source seismic attribute images (19) (Supplementary Fig. S2) and careful determination of the epicentral locations and depths (20). There, FM indicates strike-slip motion on subvertical N-S fault planes. A red traffic light protocol was triggered for one of these events during HF operations (13) and the ground motion was locally felt. Various lines of evidence (21) suggest that the depth of the  $M_w$  4.1 event (and associated cluster) lies at ~3.5 km, coincident with HF of the Duvernay Formation. (20). The lateral resolution of the stress model is ~2 km and the values for stress and  $P_p$  (Supplementary Table S2) are nearly the same for both events under the assumption they occur within or close to the Duvernay Formation. In the vicinity of the epicenters and at the center of the formation (~3.4 km depth), the model stresses are  $S_h = 65 \pm 3$  MPa;  $S_V = 84 \pm 3$  MPa, and  $P_p = 62 \pm 3$  MPa. It is worth noting that  $P_p$  substantially exceeds that expected for a normal hydrostatic pressure of

$P_H = \sim 33$  MPa. The most probable magnitude for  $S_H$  is  $\sim 124$  MPa, with the value expected to range within  $\sim 100$ - $180$  MPa to 95% confidence. Finally, the model indicates the maximum stress orientation of  $\phi = 41^\circ$ .

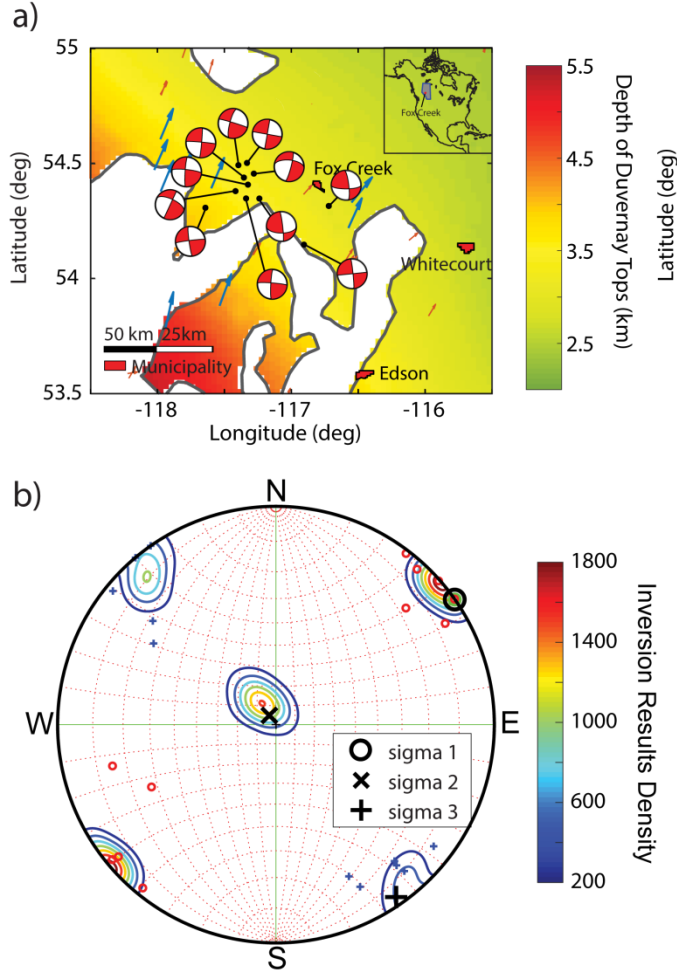


**Fig. 1. Focal mechanisms of the earthquakes analyzed in this paper.** a) The black dots show the epicentres of each earthquake. The coloured background shows the depth of the Duvernay Formation engulfed by the Leduc reefs (gray lines). Arrows show the direction of  $S_H$  determined by Borehole observations and from WSM. b) Kamb plot describing the density of stress inversion results. Black symbols show the most probable orientations for the principal components of in-situ stress. Adapted from (16).

This Andersonian stress tensor can then be resolved onto all possible planes to determine  $\sigma$  and  $\tau$  for  $SNR$  (Eqn. 1) illustrated using stereonet plots (8) (Fig. 2a-c) and compared (Fig. 2d-f) against the less optimally-oriented  $M_w$  3.9 (Jun 13, 2015) event (22). One question that arises is whether the stress data model  $P_P$ , which is measured within the intact, low-permeability rock mass through long-duration *in situ* well tests

(23), is the same as the  $P_f$  actually acting on the fault plane. For example, these faults could act as conduits to overlying and more normally pressured sediments, or they could be subject to fault valving (24). Given this uncertainty,  $SNR$  stability ranges are calculated for various  $P_f$  conditions (neglecting  $C$ ) for: i) a drained fault  $P_f = 0$  (Fig. 2a), ii) normal hydrostatic conditions  $P_f = P_H = 33$  MPa (Fig. 2b), and iii)  $P_f = P_p = 62$  MPa within the Duvernay Formation (Fig. 2c). The poles to the FM inferred fault planes for the two events are shown as red circles, and for the sake of comparison, the poles for three vertical planes that hypothetically could be associated with basement lineaments observed in seismic attribute maps (Supplementary Fig. S2) are included.

According to Eqn. 1, the fault is unstable if  $SNR > \mu$ . Consequently if  $P_f = 0$  (Fig. 2a) the  $SNR$  reaches a maximum of  $\sim 0.3$  indicating that the faults could slip only if friction is low; and suggests that the faults would likely be stable. This situation persists if  $P_f$  (Fig. 2b) is at the more normal hydrostatic gradient with low values of  $SNR \sim 0.5$  expected on the faults. However, the situation changes with larger  $P_f \approx P_p$  (Fig. 2c) where  $SNR \geq 1$  on both fault planes. This could suggest larger friction values or episodic fault valving since these faults have remained clamped (i.e., did not detectably slip) within the historical record. As might be expected, the two earthquakes ( $M_w$  3.6 & 4.1) occur on planes whose poles are close to the maximum  $SNR$  in Fig. 2, regardless of  $P_f$ , this seeming agreement warrants further examination. On the one hand, the orientations of the earthquake slip planes are independently given by the focal mechanisms as constructed from the events' radiation patterns. On the other, the orientation of the maximum  $SNR$  orientations is entirely controlled by  $\phi$ , which is also completely independently obtained from examination of borehole image logs (16, 23). Closer examination of Fig. 2 shows that here the fault planes strike at angles  $\theta = 35^\circ$  and  $37^\circ$  from  $\phi$  for the  $M_w$  3.6 and 4.1 events, respectively. This is worth pointing out because the azimuth of focal mechanism  $p$ -axes, which by definition are  $45^\circ$  from the fault plane, are often taken as a proxy for the stress directions. The smaller angle between the fault plane and  $\phi$  is consistent with frictional constraints.

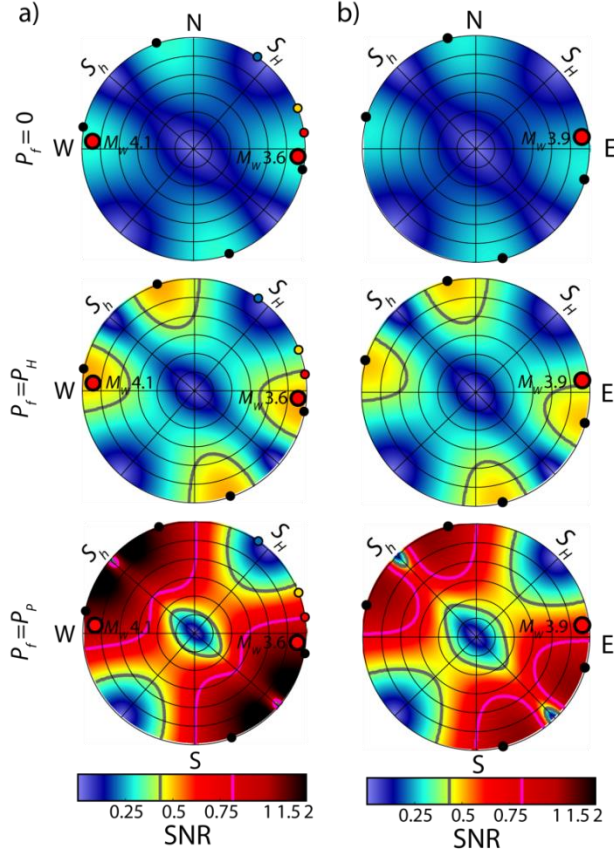


**Fig. 2. Stereonet plot for SNR neglecting  $C$ .** a-c) SNR for the  $M_w$  3.6 and 4.1 events. The large red dot represents the poles to the studied fault planes. Grey and purple lines show the contour of SNR equal to 0.4 and 0.8 respectively. Black dots show the poles of optimally oriented faults for  $\mu = 0.6$ . Small blue, yellow and red dots represent similarly coloured lineaments inferred as faults from Supplementary Fig. S1 assuming dip angle of  $90^\circ$ . d-e) SNR for  $M_w$  3.9 events. The colour scale is not linear.

### *Correlation between $P_f$ and fault's slip tendency*

Carrying out more detailed explorations of the influence of  $\mu$ ,  $P_f$  and  $C$  using only slip tendency plots, or equivalently Mohr stress diagrams, is cumbersome. Instead, the ranges of possible SNR for the fault planes for the more ( $M_w 4.1$ ) and less ( $M_w 3.9$ ) optimally oriented fault planes (Fig. 3) are calculated as functions of  $P_f$  using their respective stress tensors (Supplementary Table S1) and assuming either  $C = 0$  (red band) or  $C = 5$  MPa (green band). The height of these areas at any given  $P_f$  mostly reflects the larger distribution of expected  $S_H$  magnitudes. The same plots (Supplementary Figs. S3.1 to S3.9) for the remaining events are in the supplementary materials. Typically, workers assume  $\mu$  ranges from 0.6 to 1.0 in the upper crust (5). Here we use the range  $0.4 \leq \mu \leq 0.8$ , constrained by a variety of experimental

friction tests (see supplementary material, Table S3 and S4) on rocks similar to the clay-poor and stiff Duvernay Formation (25). There are no direct measurements of the frictional properties of these rocks currently available to our knowledge. Similarly, no direct measures of fault cohesion ( $C$ ) exist to our knowledge and researchers, too, usually ignore it completely; justification for use of these low values is provided in the supplementary materials.

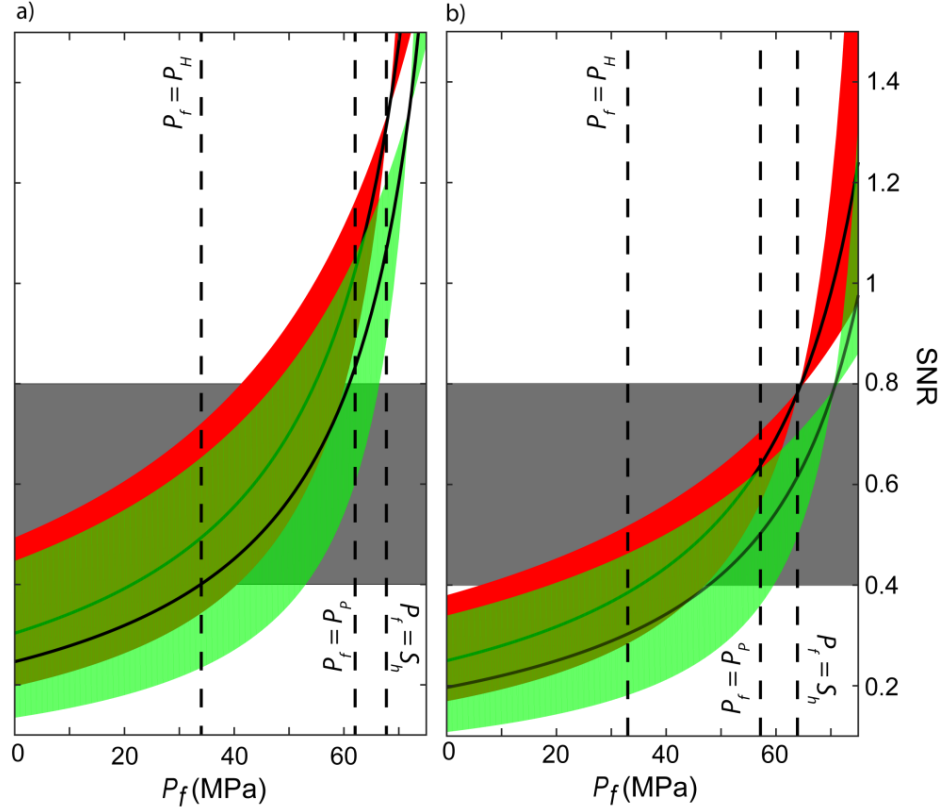


**Fig. 3. SNR vs  $P_f$  for a)  $M_w$  4.1 and b) 3.9 events.** The SNR of the earthquake's faulting plane at different fluid pressures. The red and green regions represent the SNR distributions setting, respectively, for  $C = 0$  and  $C = 5$  MPa. The width of the stripe represents the uncertainty of SNR due to different  $S_H$ , and the black lines show the calculation with the most confident value for  $S_H$ . Gray box represents the range of SNR (0.4- 0.8)

Both fault planes are likely stable if  $P_f$  remains at normal hydrostatic conditions. The poorly oriented fault plane (Fig. 3b), too, probably remains stable even at pressures exceeding the ambient  $P_p$  (57 MPa). In contrast, at the ambient  $P_p$  (62 MPa) the optimally oriented fault plane (Fig. 3a) is already unstable. The historical quiescence of this fault could be interpreted variously to mean that *i*) it is characterized by

unexpectedly high values of  $\mu$  or of  $C$ , or *ii*) that the  $P_f$  naturally active on the fault is significantly less than  $P_p$ .

Distributions for the  $SNR$  on all 11 fault planes are calculated using their individual stress tensor (Supplementary Table S2) using a Monte-Carlo procedure that incorporates the uncertainties associated with the three stress magnitudes, depths, varying  $P_f$ ,  $\mu$  and  $C$  (Fig. 4a, see supplementary material for details). The  $SNR$  distributions of these earthquakes are mostly below 0.4 in the unrealistic case where  $P_f = 0$  (Fig. 4a) reinforcing the expectation that for this extreme case all of the faults would likely remain stable. In contrast, if the faults were perfectly hydraulically connected to the Duvernay Formation such that  $P_f = P_p$ , almost all the  $SNR$  distributions shift to values well in excess of 0.8 again indicating that nearly all the faults would be unstable at ambient  $P_p$  within the reservoir.

Given that the faults appear unstable under the expected virgin formation  $P_p$ , distributions of the greatest allowable values for  $P_f$  that are necessary to maintain stability (i.e.,  $SNR \leq \mu$ ) were further explored using a Monte-Carlo approach for restricted ranges of  $\mu$  and  $C$  with the individual stress states. For most of the cases, the most probable  $P_f$  (Fig. 4b, see supplementary material for details) required to initiate slip is slightly greater than the local  $P_H$  but significantly less than the local  $P_p$ . This again indicates that the faults are likely not stable under the high ambient formation  $P_p$  and suggests that the virgin  $P_f$  acting on the faults must be lower. During stimulation, the fluid pressure required to drive a hydraulic fracture into a rock mass must at least exceed the fracture closure pressure (here  $S_h$ ), a value that in practice is readily exceeded by the actual pressures measured in the wellbore  $P_w(t)$  at the injection point during stimulation. Consequently, fluid pressures sufficiently high to initiate slip are present within the system during stimulation, although the actual fluid pressures delivered to the fault through the induced fracture network from the borehole remain highly uncertain. Non-double couple focal mechanism components anecdotally suggest fluid inflow into the fault during the earthquake (22). Meta-analysis of the microseismic literature suggests that most HF extend laterally no more than 400 m with excursions to nearly 900 m from the injection point (26); and this may provide some insight on the distance fluid pressures could be



transmitted during an HF stimulation. That said, model-derived estimates depend on having knowledge of many largely unconstrained factors controlling fracture and fault geometries and fluid transport. Poroelastic stresses, too, may contribute to the stress state on the fault planes at initiation uncertain in these formations but numerical (27) and analytical (28) simulations suggest their influence on the  $SNR$  is a small fraction relative to  $P_f$ .

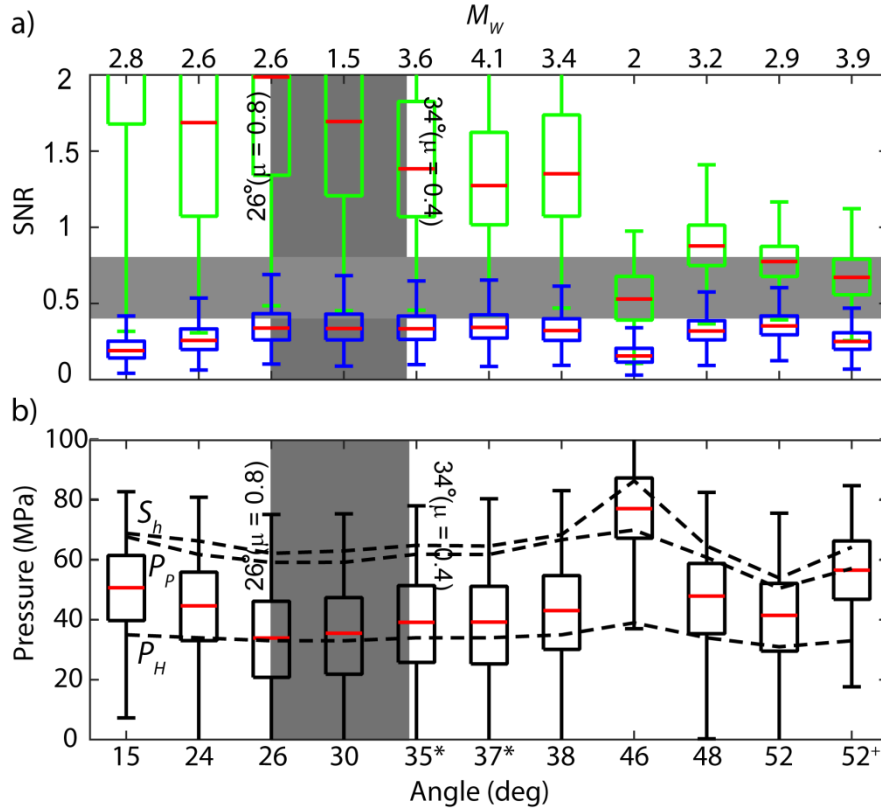


**Fig. 4. Monte-Carlo calculations versus angle  $\psi$  of a)  $SNR$  distributions on the fault planes calculated assuming  $P_f = 0$  (blue) and  $P_f = P_p$  (green), boxes indicate the 25<sup>th</sup> and 75<sup>th</sup> percentile limits of the probability density functions, and the red lines indicate the most probable  $SNR$  value for each case. b) The fluid pressures needed to activate the faults, boxes indicate the 25<sup>th</sup> and 75<sup>th</sup> percentile limits of the probability density functions, and the red lines indicate the most probable critical  $P_f$  value. Black dashed lines represent the fracture closure pressure (equal to  $S_h$ ), measured virgin  $P_p$  and depth-dependent normal hydrostatic pressure  $P_H$ . Shaded gray zones in both panels indicate suggested  $SNR$  and optimal orientation angle ranges.**

In Fig. 4, the difference local angle difference  $\psi = S - \phi$  between fault strike  $S$  and the  $S_H$  direction (Supplementary Table S1) is intentionally chosen as the independent variable to emphasize that the planes of weakness are not necessarily all optimally aligned with the stress field. The suggested range  $0.4 \leq \mu \leq 0.8$  delimits the optimal range  $34^\circ \geq \psi \geq 26^\circ$  highlighted in Fig. 4; which almost all of the

events fall outside of. This observation could have multiple interpretations. The most likely explanation is that more optimally oriented planes of weakness are absent at these locations; slip instead occurs on those pre-existing faults that are closest to unstable but not perfectly aligned with the stress field. Another interpretation is that the slip does occur on the real fault planes that are optimally oriented, but the FM planes or values of stress (retaining the Andersonian assumption) are uncertain.

In summary, we analyzed the slip-tendencies along faults activated by hydraulic fracture stimulations in a localized area of NW Alberta, Canada using a recently developed quantitative model for the full stress tensor and the formation pore fluid pressures  $P_p$  within the highly over-pressured Duvernay Formation. Assuming reasonable ranges for fault friction and cohesion, nearly all of the slip-planes studied would be unstable at the measured ambient formation pore fluid pressures  $P_p$ . This instability persists although most of the slip-planes are not expected to be optimally oriented with respect to the prevailing stress directions. That this area was historically aseismic prior to hydraulic fracturing operations, however, indicates that the natural fluid pressures within the fault zone must be lower unless unexpectedly large frictions or cohesions exist; and Monte-Carlo simulations suggest that generally, the most probable critical fluid pressures lie closer to the normal hydrostat. As hydraulic fracturing stimulations generally attempt to maintain fluid pressures above  $S_h > P_p$ , the potential to convey in excess of a critical pressure to the surrounding formation exist, although actually quantitatively estimating the critical pressure is difficult. The lower pressures within the faults suggest that they may serve to provide conduits for migration of hydrocarbons out of the low permeability Duvernay Formation to the overlying siliclastic formations and may be consistent with the critically stressed crust hypothesis (29). The results here highlight the challenges confronting researchers hoping to understand the physics of earthquake rupture by artificially initiating fault slip (30).

## **Reference**

1. G. R. Foulger, M. P. Wilson, J. G. Gluyas, B. R. Julian, R. J. Davies, Global review of human-induced earthquakes. *Earth-Sci. Rev.* **178**, 438-514 (2018).

2. J. Rice, A. L. Ruina, Stability of steady frictional slipping. *Journal of Applied Mechanics* **50**, 343-349 (1983).
3. M. L. Blanpied, D. A. Lockner, J. D. Byerlee, Frictional slip of granite at hydrothermal conditions. *Journal of Geophysical Research: Solid Earth* **100**, 13045-13064 (1995).
4. M. Scuderi, C. Collettini, C. Marone, Frictional stability and earthquake triggering during fluid pressure stimulation of an experimental fault. *Earth and Planetary Science Letters* **477**, 84-96 (2017).
5. J. Byerlee, in *Rock friction and earthquake prediction*. (Springer, 1978), pp. 615-626.
6. M. King Hubbert, W. W. Rubey, Role of fluid pressure in mechanics of overthrust faulting: I. Mechanics of fluid-filled porous solids and its application to overthrust faulting. *Geological Society of America Bulletin* **70**, 115-166 (1959).
7. C. Raleigh, J. Healy, J. Bredehoeft, An experiment in earthquake control at Rangely, Colorado. *Science* **191**, 1230-1237 (1976).
8. A. Morris, D. A. Ferrill, D. B. Henderson, Slip-tendency analysis and fault reactivation. *Geology* **24**, 275-278 (1996).
9. G. M. Atkinson *et al.*, Hydraulic fracturing and seismicity in the Western Canada Sedimentary Basin. *Seismological Research Letters* **87**, 631-647 (2016).
10. R. Schultz, G. Atkinson, D. Eaton, Y. Gu, H. Kao, Hydraulic fracturing volume is associated with induced earthquake productivity in the Duvernay play. *Science* **359**, 304-308 (2018).
11. D. W. Eaton, R. Schultz, Increased likelihood of induced seismicity in highly overpressured shale formations. *Geophysical Journal International* **214**, 751-757 (2018).
12. R. Schultz *et al.*, Linking fossil reefs with earthquakes: Geologic insight to where induced seismicity occurs in Alberta. *Geophysical Research Letters* **43**, 2534-2542 (2016).
13. T. Shipman, R. MacDonald, T. Byrnes, Experiences and learnings from induced seismicity regulation in Alberta. *Interpretation* **6**, SE15-SE21 (2018).
14. R. Schultz, R. Wang, Y. J. Gu, K. Haug, G. Atkinson, A seismological overview of the induced earthquakes in the Duvernay play near Fox Creek, Alberta. *Journal of Geophysical Research: Solid Earth* **122**, 492-505 (2017).
15. O. Heidbach, M. Rajabi, K. Reiter, M. Ziegler, World stress map 2016. *Science* **277**, 1956-1962 (2016).
16. L. Shen, D. R. Schmitt, K. Haug, Quantitative constraints to the complete state of stress from the combined borehole and focal mechanism inversions: Fox Creek, Alberta. Preprint at, <https://arxiv.org/abs/1902.05682> (2019).
17. T. Terakawa, E. Hauksson, Absolute Stress Fields in the Source Region of the 1992 Landers Earthquake. *Journal of Geophysical Research: Solid Earth* **123**, 8874-8890 (2018).
18. V. Vavryčuk, Iterative joint inversion for stress and fault orientations from focal mechanisms. *Geophysical Journal International* **199**, 69-77 (2014).
19. S. Chopra *et al.*, Seismic reservoir characterization of Duvernay shale with quantitative interpretation and induced seismicity considerations—A case study. *Interpretation* **5**, T185-T197 (2017).

20. R. Wang, Y. J. Gu, R. Schultz, M. Zhang, A. Kim, Source characteristics and geological implications of the January 2016 induced earthquake swarm near Crooked Lake, Alberta. *Geophysical Journal International* **210**, 979-988 (2017).
21. D. W. Eaton *et al.*, Induced Seismicity Characterization during Hydraulic-Fracture Monitoring with a Shallow-Wellbore Geophone Array and Broadband Sensors. *Seismological Research Letters* **89**, 1641-1651 (2018).
22. R. Wang, Y. J. Gu, R. Schultz, Y. Chen, Faults and Non-Double-Couple Components for Induced Earthquakes. *Geophysical Research Letters* **45**, 8966-8975 (2018).
23. L. Shen, D. R. Schmitt, K. Haug, "Measurements of the States of In Situ Stress for the Duvernay Formation near Fox Creek, West-Central Alberta," *AER/AGS Report* (Alberta Energy Regulator / Alberta Geological Survey, 2018).
24. R. H. Sibson, Conditions for fault-valve behaviour. *Geological Society, London, Special Publications* **54**, 15-28 (1990).
25. O. N. Ong, D. R. Schmitt, R. S. Kofman, K. Haug, Static and dynamic pressure sensitivity anisotropy of a calcareous shale. *Geophys. Prospect.* **64**, 875-897 (2016).
26. M. Wilson, F. Worrall, R. Davies, S. Almond, Fracking: How far from faults? *Geomechanics and Geophysics for Geo-Energy and Geo-Resources* **4**, 193-199 (2018).
27. K. Chang, P. Segall, Injection-induced seismicity on basement faults including poroelastic stressing. *Journal of Geophysical Research: Solid Earth* **121**, 2708-2726 (2016).
28. P. Segall, S. Lu, Injection-induced seismicity: Poroelastic and earthquake nucleation effects. *Journal of Geophysical Research: Solid Earth* **120**, 5082-5103 (2015).
29. J. Townend, M. D. Zoback, How faulting keeps the crust strong. *Geology* **28**, 399-402 (2000).
30. H. M. Savage *et al.*, Scientific exploration of induced seismicity and stress (SEISMS). *Scientific Drilling* **23**, 57-63 (2017).

### ***Acknowledgement***

Earlier components of the work were supported by Helmholtz-Alberta Initiative and NSERC Discovery Grant. The authors declare no competing interests.

## ***Methods***

### ***Synopsis of quantitative stress model***

The predictive quantitative stress model for the area encompassing the 11 induced events is developed (1) using publicly archived field data (2). The stress model assumes an Andersonian stress state with the vertical normal stress being the vertical principal compression  $S_V$ , and including the greatest  $S_H$  and least  $S_h$  horizontal compressions within a Cauchy stress tensor  $T$

$$T = \begin{bmatrix} S_H & 0 & 0 \\ 0 & S_V & 0 \\ 0 & 0 & S_h \end{bmatrix} = \begin{bmatrix} \sigma_1 & 0 & 0 \\ 0 & \sigma_2 & 0 \\ 0 & 0 & \sigma_3 \end{bmatrix} \quad (S1)$$

oriented by the trend azimuth  $\phi$  of  $S_H$  measured counter-clockwise from geographic  $N$  within a north-east-down co-ordinate system. The model also includes estimates of formation pore pressure  $P_p$ . Compressions and fluid pressures have positive sign.

Values that are directly determined include:

### ***Stress orientation $\phi$***

$\phi$  as measured from observations and borehole breakouts and drilling-induced tensile fractures from 21 sets of oriented ultrasonic image logs, and supplemented using local directions from the World Stress Map (3) database and additional data reported by Haug and Bell (4) to create an interpolated map (Supplementary Fig. S1a). Stress directions are assumed to remain constant with depth at a given location.

### ***Vertical Stress $S_V$***

$S_V$  as determined by vertical integration of 1181 individual density logs followed by a 3D interpolation and corrected for surface topography. The interpolated  $S_V$  magnitudes on the top of the Duvernay Formation are shown in Supplementary Fig. S1b.

### ***Minimum horizontal stress $S_h$***

$S_h$  as determined from estimates of the hydraulic fracture closure pressures from 30 industrial pressure tests. These tests are often referred to as diagnostic fracture interpretation test (DFIT) with details documented (1). It is important to note that all of these measurements occurred within only within the Duvernay Formation and these values interpolated to the Duvernay Formation are shown in Supplementary Fig. S1c. Simple linear regression of these observed  $S_h$  versus depth  $z$  gives:

$$S_h(z) = 32.1 \pm 3.8 \frac{kPa}{m} z - 41.8 \pm 12.3 MPa \quad (S2)$$

and the tangent gradient of this relation is used to extrapolate  $S_h$  vertically away from the center of the Duvernay Formation within the predictive model.

### ***Formation Pore pressure $P_p$***

$P_p$  as estimated from extrapolation of borehole pressure decay curves to infinite time in a larger set of industrial pressure tests also taken from the Duvernay Formation (1) with the interpolated map shown in Fig. 2d. Again, the simple linear regression of the observed  $P_p$  versus  $z$  gives

$$P_p(z) = 29.1 \pm 7.2 \frac{kPa}{m} z - 40.0 \pm 46.7 MPa \quad (S3)$$

whose tangent gradient is used to extrapolate  $P_p$  vertically away from the center of the Duvernay Formation within the predictive model.

### ***Maximum horizontal stress $S_H$***

$S_H$  magnitudes were not successfully obtained directly from the borehole data. Alternatively, we first carried out a standard inversion of the 11 focal plane mechanisms described in Schultz et al. (5, Supplementary Table S1) using Vavryčuk (6) algorithm to provide a distribution of values for the regional shape factor  $R$

$$R = \frac{\sigma_1 - \sigma_2}{\sigma_1 - \sigma_3} = \frac{S_H - S_V}{S_H - S_h} \quad (S4)$$

applicable to the strike-slip faulting regime in the area. Ten-thousand random realizations are run with varying inputs to account for uncertainties to the input stresses and focal plane solutions, with a mean random error of  $\pm 10^\circ$  is assigned to the strike, dip and rakes of the solutions. The inversion results show that the most probable intermediate stress ( $\sigma_2$ ), considering that the three principal components of a stress tensor have to be orthogonal to each other, only plunges slightly away from the vertical axes ( $< 5^\circ$ , Fig. 2) suggesting the validity of the assumed Andersonian (7) states of stress.

This analysis gave a most probable value  $R = 0.67$  with the 95% confidence interval  $0.46 \leq R \leq 0.84$ . Following Terakawa and Hauksson (8), a distribution of local depth-depth dependent  $S_H$  may then be calculated from the model  $S_V$  and  $S_h$  thus completing the determination of  $T$  at each epicentre. A Matlab<sup>TM</sup> program *threeD\_stress\_duvernay.m* is provided by Shen et al. (1) allowing extraction of stress information ( $[S_H, S_V, S_h]$  and  $P_P$ ) for an input location specified with Latitude, Longitude and depth in an area containing the HF-induced earthquakes and as mapped in Supplementary Fig. S1. This program provided the stress values with uncertainties shown in Supplementary Table S2.

### ***Slip tendency analysis***

The slip tendency for an arbitrarily oriented plane is quantified by the value  $SNR$  of Equation 1. Following (9), the  $SNR$  for all possible fault planes are displayed as contours within a stereonet plot. This necessitates that both the shear  $\tau$  and normal  $\sigma$  tractions be calculated for the given stress tensor  $T$  with known azimuth  $\phi$  using well-known equations in continuum mechanics (see review in Schmitt et al. (10)). Examination of Equation 1 shows that knowledge of both the fluid pressure  $P_f$  and the fault cohesion  $C$  are required. In Fig. 2 in the main text and Supplementary Figs. S3.1a through S3.9a the three stability stereonet plots are calculated for illustrative cases of  $P_p = 0$ , of  $P_p$  equal to that expected for the normal hydrostatic pressure at the particular depth, and of  $P_p$  that predicted by the model described above.  $C$  was set equal to 0 in all cases.

For a given  $T$ , the Matlab™ code `stress_on_plane.m` calculates the  $\tau$  and  $\sigma$  over the range of possible planes with the resulting  $SNR$  displayed by `sternet_plot.m`. The  $SNR$  for each of the presumptive fault planes (Supplementary Table S1) are also calculated separately versus the fluid pressure  $P_f$  for two cases assuming  $C = 0$  (red band), or  $C = 5$  MPa (green band) and for the range of stress tensors  $T$  possible according to the stress model (Fig. 3 in main text and Supplementary Figs. S3.1b to S3.9b).

### ***Analyses on seismic attributes derived lineaments***

Supplementary Fig. S2 shows the horizontal slice of the seismic attributes (most-negative curvature), at the depth of the basement, from a 3D seismic survey conducted in an area encompassing two moderate magnitudes earthquakes (11). The location of Supplementary Fig. S2 was not reported in Chopra et al. (11) and it is inferred that, by cross-referencing with reported earthquake's source mechanisms, these two events marked on Supplementary Fig. S2 are corresponding to the  $M_w$  3.6 and 4.1 events compiled in Schultz et al. (5) and analyzed in Fig. 2. The seismic data plotted in Fig S1 remains proprietary at the moment of this writing. Stability analysis in Fig 2 utilizes the average stress values calculated for these two events with coordinates reported in Schultz et al. (5).

Assuming the interpreted lineaments in Supplementary Fig. S2 represent actual faults, of the two dominant transtentional fault orientations (i.e., NNW-SSE and NE-SW, Supplementary Fig. S2), only the NNW-SSE faults appear to be within the spectrum of instability (Fig. 2a), while the NE-SW is not. This is in agreement with the reported induced earthquake fault orientations that produced slip nucleation. On the other hand, one fault identified (oriented NWW-SEE), strikes at a stable angle of  $\sim 90^\circ$  from  $S_H$ , is observed to be non-seismogenic despite proximity to the HF wells. Faults which are more optimally oriented (see Fig. 2) but further away from the seismogenic HF wells are not activated either.

Though the stability analysis provided results in agreement with the observed, or lack of, seismicities, along the lineaments features, it is uncertain if these features represent actual faults within the Duvernay Formation. The interpretation presented by Chopra et al. (11) is made assuming that the faulting in the sedimentary layers of the study area is basement controlled (12).



### ***Expectations for $C$ and $\mu$***

In previous studies,  $C$  is often neglected as an earthquake generally reactivates on an existing fault with assumed negligible cohesion. Such assumption is supported by most reported lab experiments (13).

Though the residual strength of the fault, post shear failure, is measured to be very small, fault regains strength after a period of healing. Earlier researchers debated whether such strength recovery is in forms of friction (14-16) or cohesion (17, 18). Distinguishing the effects of cohesion and friction as the results of fault healing observed in the lab experiment is also reported to be difficult (19). Regardless, measured post shear failure cohesion on clay-rich material is generally small (20-22). Sone and Zoback (23) observed that the creep rate of the shale positively correlates with the clay content of the testing sample. Shales from Duvernay and other Paleozoic formations in Western Canada Sedimentary Basin generally has low clay content and would have lesser cohesion than the clay-rich shales. Though larger numbers ( $> 20$  MPa) have been reported (17) from fault healing experiment, those numbers are measured at high temperature ( $> 800$  °C) and high-pressure ( $> 175$  MPa) environment. In this study, a conservative range of  $C$  between 0 – 5 MPa is considered. This admittedly requires more study.

Similarly, values for the in-situ friction static coefficient  $\mu$  are not reported. Though a default  $\mu$  of 0.6 - 1 is often assumed for many geomechanical studies (9, 24, 25), laboratory measurements conducted on the different material composition of fault gouge at different testing environments observed a wide range of the  $\mu$ . A brief compilation on the reported  $\mu$  known to the authors, and with mineral composition relevant to this study, is provided in the supplementary material (Table S3, 26-40). X-ray diffraction analysis (Table S4) on five of the samples extracted in-situ from boreholes drilled targeting or through the Duvernay formation shows the significant components of Quartz and Calcite, with a smaller amount of clay. By the friction measurements reported on samples with comparable mineral composition and normal pressures, the  $\mu$  of the fault studied in this analysis is selected between 0.4 – 0.8.

### ***Monte-Carlo Simulation of SNR for different $P_f$ (for Fig. 4a)***

The Monte-Carlo calculation used in obtaining the  $P_f$  whisker-plot distributions of Fig. 4b in the main text are described here. Equation 1 had defined the SNR which can be calculated with knowledge of the complete stress tensor described by  $S_h$ ,  $S_v$ ,  $S_H$ ,  $\phi$  and  $P_p$ . The Monte-Carlo simulation is excited with a large number of realizations ( $n = 5000$ ) and ranges of stress components constrained by uncertainties reported (1).

Uncertainties caused by varying epicentre's depths are accounted for by assuming a variation of  $\pm 500$  m relative to the center of the Duvernay Formation within which the events are most likely to have occurred (41). In each realization,  $S_h$  and  $S_v$  are corrected to the randomly selected depth with their tangent slopes discussed earlier. Random  $S_H$  finally calculated based on the statistical distribution of the local stress shape-ratio (ranging between 0.46-0.84, see Supplementary Fig. S2) and previously generated  $S_h$  and  $S_v$ . We ignore uncertainties in  $\phi$  and in the orientations of the focal mechanism solutions due to the lack of reported values. A Matlab<sup>TM</sup> function monte\_carlo\_stability.m is provided to perform such analysis. With input parameters for each earthquake shown in Table S1 and stress values in Table S2, this function is adapted in monte\_carlo\_stability\_runit.m to plot Fig. 4

### ***Monte-Carlo Simulation of $P_f$ required to initiate slip (for Fig. 4b)***

Similar to Figure 4a, the Monte-Carlo method is adapted to calculate the probability distribution of  $P_f$  needed to activate the faults by rearranging Equation 1 in the main text:

$$P_f = \sigma - (\tau - C) / \mu \quad (S5)$$

Calculation of Eqn. S5 utilizes the previously calculated 5000 Shear Stress ( $\tau$ ) and normal pressure ( $\sigma$ ) values along with five-thousand randomly generated  $C$  (0 – 5 MPa) and  $\mu$  (0.4 – 0.8). The Matlab<sup>TM</sup> function monte\_carlo\_stability.m and script monte\_carlo\_stability\_runit.m also perform this analysis.

It is notable that there is one exceptional earthquake case which appears to be stable, given the determined in-situ stress conditions and fault stability analysis in this study (Fig. 4) with stability analysis for this

particular case plotted in Supplementary Fig. S3.9. The pressures required to activate the fault is probably higher than the  $P_p$  under reasonable assumption. However, SNR of this fault will likely exceed 0.8, the upper bound of our test range of  $\mu$ , when  $P_f$  gets close to  $S_h$ , the minimum pressures needed to create fractures during HF operations. Additionally, this case also displayed seismologically distinct earthquake cluster properties (5). First, events in this region exhibited rotated focal mechanisms with larger normal component of slip than their predominantly N-S strike-slip counterparts. Second, these clusters appeared to have small inter-well communication – a feature not observed for other HF completions in the Duvernay. Last, these clusters showed distinctly different statistics (large b-value), with comparatively numerous small magnitude events (5). Explanations for these discrepancies could be related to a local stress heterogeneity or stress rotation in this area that was not captured regionally. On the other hand, the relatively small magnitude of events in this cluster could have also contributed to larger errors in focal mechanism determinations. Higher resolution datasets could help better constrain this anomaly, however.

### *Supplementary Tables and Figures*

**Table S1.** A total of 11 earthquakes recorded by the regional seismometer network with well resolved focal mechanisms are analyzed in this study. The abbreviated column names stand for  $M_W$  – Magnitudes, Lat – Latitude (deg), Lon – Longitude (deg), Dep – Depth (km), S – Strike Angle N-E (deg), D – Dip angle (deg), R – Rake angle (deg).

$M_W$	Date	Lat	Lon	Dep	S	D	R
2.8	8-Aug-15	54.38	117.4	3.5	25	90	-145
3	19-Aug-15	54.46	117.27	3.3	15	79	-139
2.6	18-Jan-15	54.50	117.38	3.4	195	70	175
1.5	17-Nov-15	54.51	117.32	3.3	10	90	180
4.1*	12-Jan-16*	54.41	117.31	3.4	184	81	166
3.6*	23-Jan-15*	54.44	117.34	3.4	5	85	-175
3.4	14-Jan-15	54.35	117.32	3.5	183	81	172
3.2	10-Feb-15	54.35	117.22	3.4	354	82	140
2.9	3-Dec-15	54.33	116.71	3.1	353	74	157
3.9 <sup>+</sup>	13-Jun-15 <sup>+</sup>	54.16	116.89	3.3	354	85	-180
2	22-Sep-15	54.31	117.62	3.9	172	82	174

\*Event analysis shown as examples in Fig. 2a and 3a; <sup>+</sup>Event analyzed as an example in Fig. 2b and 3b.

**Table S2.** States of in-situ stress at the epicentral locations of the earthquakes. The abbreviated column names stand for  $M_W$  – Magnitudes,  $S_H$  AZ – N-E orientation of maximum horizontal compressional stress (deg),  $S_h$  – Minimum horizontal stress (MPa),  $S_V$  – Vertical stress (MPa),  $S_H$  – Maximum horizontal stress (MPa) constrained using the shape-ratio evaluated through stress inversion technique.  $S_H$  max – Maximum  $S_H$  constrained with borehole observation.  $P_p$  – Apparent pore pressures of the unconventional shale oil/gas reservoir nearby.

$M_W$	$S_H$ AZ $\phi$	$S_H$	$S_H$ max	$S_H$ min	$S_h$	$S_V$	$P_p$
2.8	40	122.5	179.0	100.4	68.5 $\pm$ 2.2	86.4 $\pm$ 2.6	67.8 $\pm$ 2.2
3	41	122.1	182.7	97.4	61.9 $\pm$ 2.8	81.8 $\pm$ 2.5	59.2 $\pm$ 2.8
2.6	39	117.5	166.6	96.3	66.0 $\pm$ 2.5	83.2 $\pm$ 2.4	61.8 $\pm$ 2.5
1.5	40	117.6	172.2	94.6	62.7 $\pm$ 2.9	80.9 $\pm$ 2.5	59.2 $\pm$ 2.9
4.1*	41	122.4	180.0	98.9	64.5 $\pm$ 2.5	83.9 $\pm$ 2.7	62.5 $\pm$ 2.5
3.6*	40	125.3	185.3	100.3	64.7 $\pm$ 2.2	84.7 $\pm$ 2.7	62.1 $\pm$ 2.2
3.4	41	125.9	184.3	102.3	68.1 $\pm$ 2.6	87.3 $\pm$ 2.7	66.7 $\pm$ 2.6
3.2	42	126.8	188.6	101.2	64.3 $\pm$ 2.3	85.1 $\pm$ 2.1	60.9 $\pm$ 2.3
2.9	45	122.7	188.9	95.0	53.7 $\pm$ 1.9	76.6 $\pm$ 2.3	50.5 $\pm$ 1.9
3.9 <sup>+</sup>	46	112.6	163.7	92.6	63.9 $\pm$ 1.6	80.1 $\pm$ 2.3	57.2 $\pm$ 1.6
2	38	119.9	155.2	104.9	86.0 $\pm$ 1.8	97.3 $\pm$ 2.8	70.00 $\pm$ 1.8

\*Event analysis shown as examples in Fig. 2a and 3a; <sup>+</sup>Event analyzed as an example in Fig. 2b and 3b.

**Table S3.** A summary of previous friction test on rocks with mineral composition related to this study

Author(s)	Mineral Composition	Pressure	$\mu$
Kohli and Zoback (26)	various shale	10 - 30 MPa	0.6 -0.79
Scuderi et al. (27)	granular quartz powders	2-18 MPa	0.56-0.58
Gu and Wong (28)	Quartz	50-190 MPa	0.6-0.8
Crawford et al. (29)	Quartz-Kaolinite Mixtures	5-50 MPa	0.5-0.65
Tembe et al. (30)	quartz-clay	40 MPa	0.5-0.75
Takahashi et al. (31)	Quartz and clay	75 MPa	0.53-0.68
Scott et al. (32)	Granular quartz	25 MPa	0.37 – 0.66
Ikari et al. (33)	Quartz + Clay	20 -50 MPa	0.6-0.7
Ikari et al. (34)	Quartz + Clay	4-100 MPa	0.5-0.6
Morrow et al. (35)	Quartz and Calcite	100 MPa	0.4 -0.85
Nakatani and Scholz (36)	Quartz	60 MPa	0.5-0.7
Marone et al. (37)	Quartz	50-190 MPa	0.5–0.65
Logan and Rauenzahn (38)	Quartz + Clay	25-70 MPa	0.5-0.6
Weeks and Tullis (39)	Dolomite marble	50-75 MPa	0.56-0.58
Samuelson and Spiers (40)	quartz + Clay	35 MPa	0.47-0.61

**Table S4.** Mineral composition (in percentage by weight) of the Duvernay shale determined through Xray-Diffraction analysis. The abbreviated column names stand for: Q – Quartz, C – Calcite, A – Anorthite, O – Orthoclase, K – Kaolinite, P-Pyrite, A2 – Ankerite, D – Dolomite, M – Muscovite/Illite, A3- Albite

Formation	Q	C	A	O	K	P	A2	D	M	A3
Duvernay	36.3	12.8	4.2	16.5		1.7	10.3	6.4	11.4	2.9
Duvernay	40.3	7.6	4.2	7.1		0.7	9.3	16.7	10.8	
Duvernay	14.1	35	3.4	11.6		3.6	3.8	22.3	6.2	6
Duvernay	40.2	12.4	6.1	10.1	0.8	2.3	6.9	5.4	9.3	
Beaverhill	37.9	14.2	4.1	11.8		3.5	4.6	3.4	19.7	

## Supplementary Figures

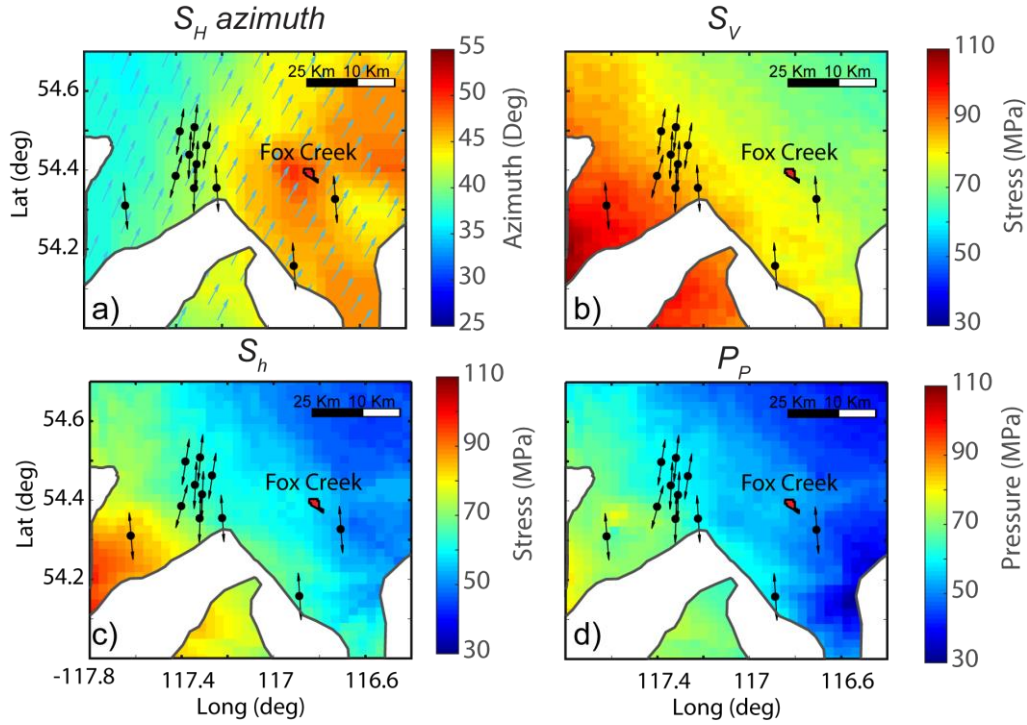


**Fig. S1.** Interpolated maps at the top of the Duvernay Formation of the directly measured stress tensor components of a)  $S_H$  trend azimuth  $\phi$  in colormap with directions shown by cyan arrows at selected grid points, b) vertical compression  $S_V$ , c) least horizontal compression  $S_h$  and d) formation pore pressure  $P_P$ . Black arrows and dots indicate strike angles and epicentres of the 11 events studied. White unfilled zones indicate areas where Duvernay Formation is replaced by Devonian Leduc reef structures.

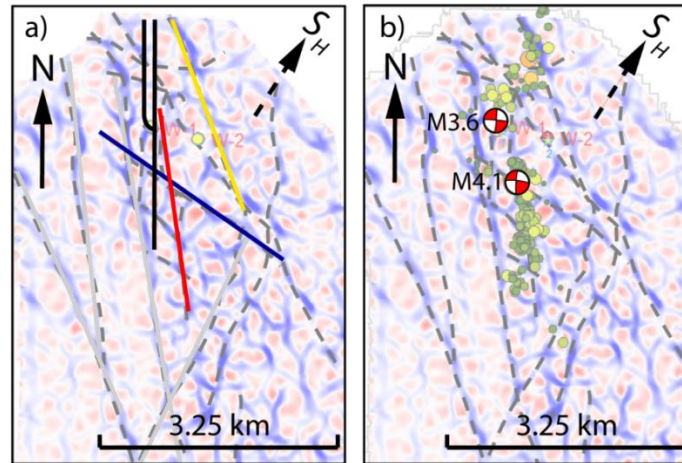


**Fig. S2.** Fault inferred through reflection seismic survey with background colours represent the attributes used for seismic interpretation. a) Black lines represent the HF wells trajectories. Coloured lines represent lineaments interpreted as faults with. b) Beach balls show the resolved focal mechanisms for earthquakes  $M_W$  3.6 and  $M_W$  4.1. In both a) and b) dashed black arrows represent the orientation of  $S_H$ .

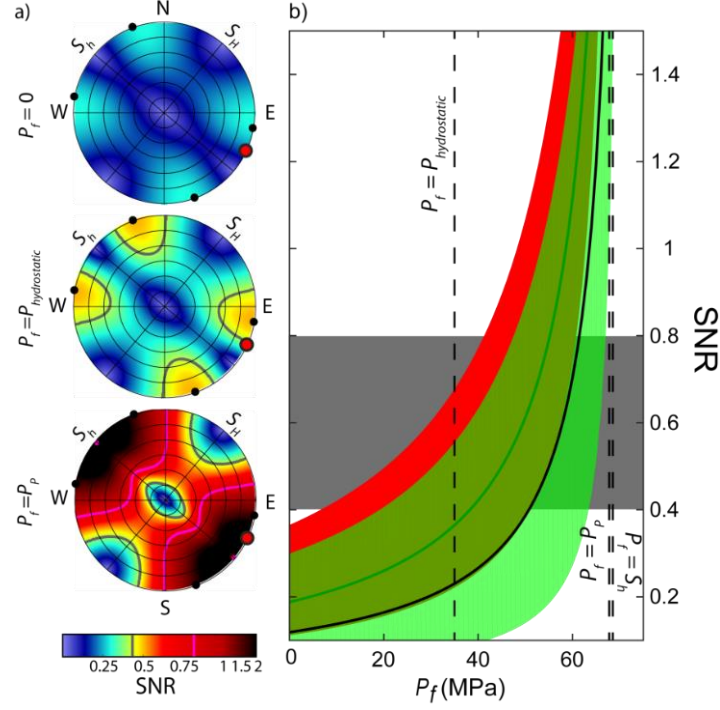


**Fig. S3.1.** Stability analysis for  $M_W 2.8$  (Aug 8, 2015) event in Table S1. a) Steronet plot for  $SNR$  neglecting  $C$  in cases of  $P_f = 0$ ,  $P_f$  equals expected hydrostatic pressure ( $P_H$ ),  $P_f = P_p$ . Red dots represent the pole of the earthquake's faulting plane. Gray and red contours represent  $SNR$  equal to 0.4 and 0.8. Black dots show the poles of faults optimally oriented for slipping assuming  $\mu = 0.6$ . b) The  $SNR$  of the earthquake's faulting plane at different fluid pressures. The red band shows the  $SNR$  without accounting for  $C$  and the green band accounts for  $C = 5$  MPa. The width of the stripe represents the uncertainty of  $SNR$  due to different  $S_H$ , and the black lines show the calculation done with the most confident value for  $S_H$ . Gray box represents the range of  $SNR$  (0.4- 0.8).

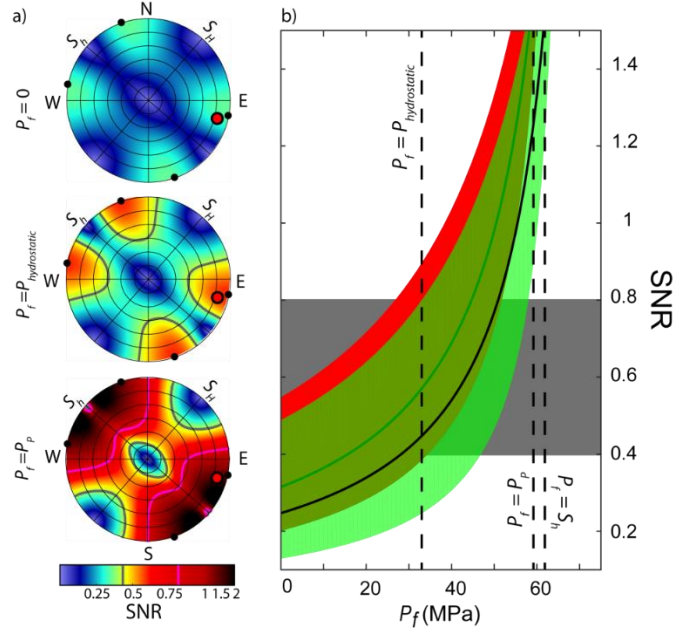


**Fig. S3.2.** Stability analysis for  $M_W 3$  (Aug 19, 2015) event in Table S1.



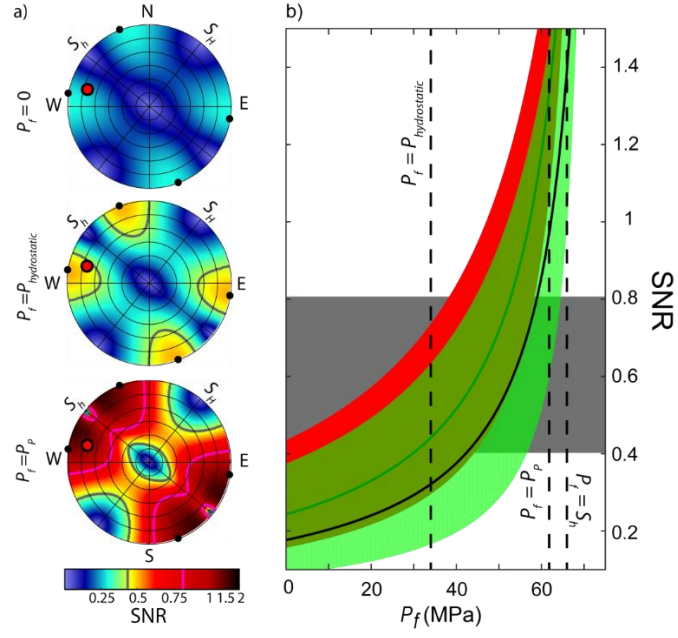


**Fig. S3.3.** Stability analysis for  $M_W$  2.6 (Jan 18, 2015) event in Table S1.

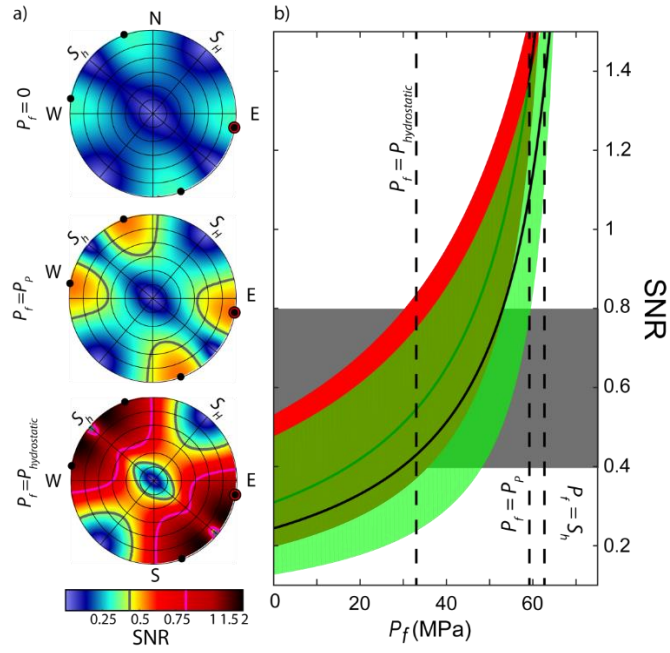


**Fig. S3.4.** Stability analysis for  $M_W$  1.5 (Nov 17, 2015) event in Table S1.

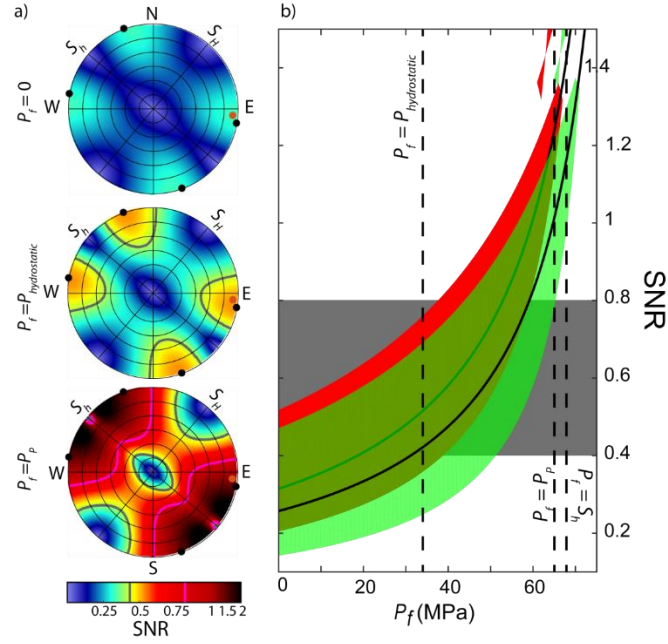


**Fig. S3.5.** Stability analysis for  $M_w$  3.6 (Jan 23 2015) event in Table S1.

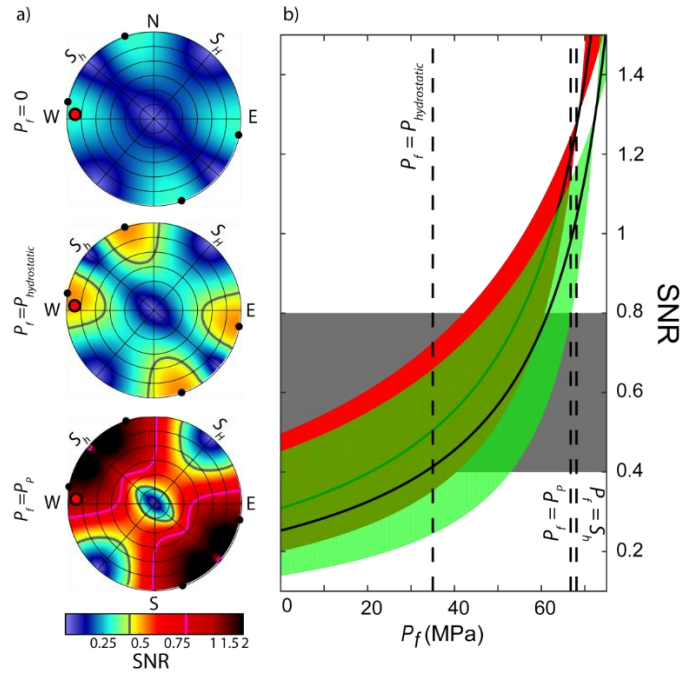


**Fig. S3.6.** Stability analysis for  $M_w$  3.4 (Jan 14, 2015) event in Table S1.

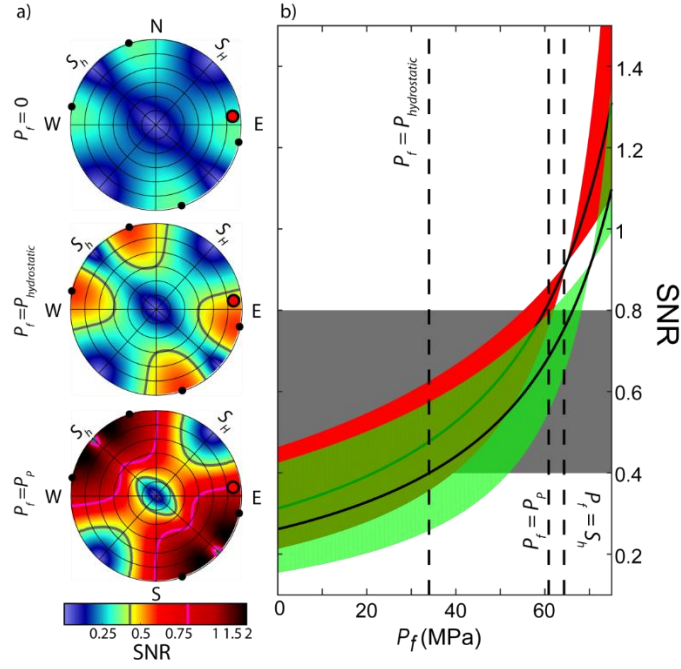


**Fig. S3.7.** Stability analysis for  $M_W$  3.2 (Feb 10, 2015) event in Table S1.

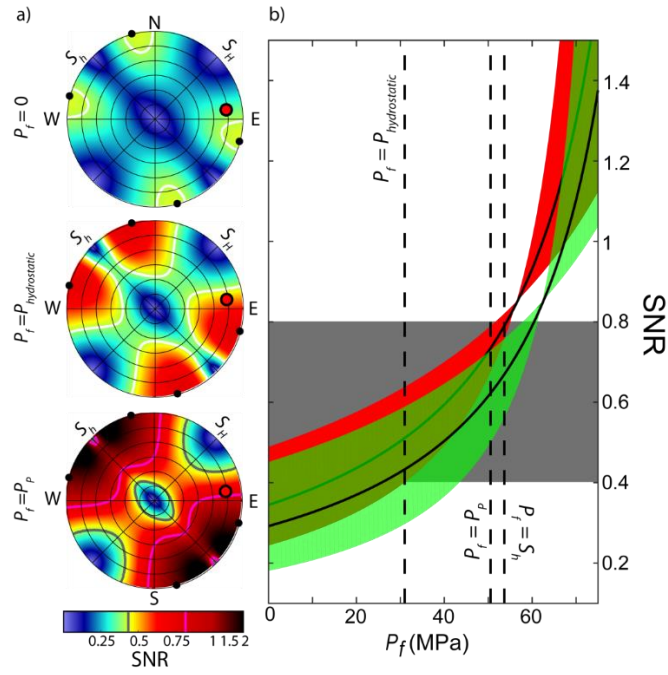


**Fig. S3.8.** Stability analysis for  $M_W$  2.9 (Dec 3, 2015) event in Table S1.

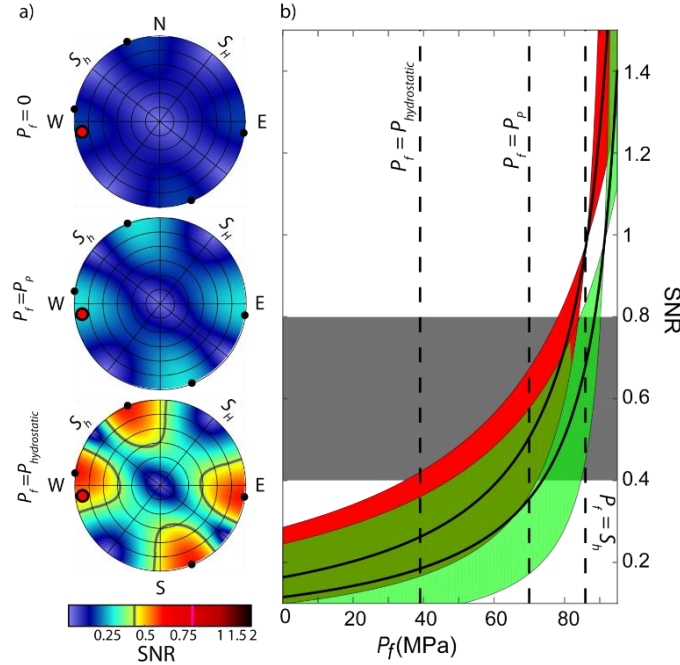


**Fig. S3.9.** Stability analysis for  $M_w$  2 (Sep 22, 2015) event in Table S1.

#### **References for Methods and Supplementary tables & figures**

1. L. Shen, D. R. Schmitt, K. Haug, Quantitative constraints to the complete state of stress from the combined borehole and focal mechanism inversions: Fox Creek, Alberta. Preprint at, <https://arxiv.org/abs/1902.05682> (2019).
2. L. Shen, D. R. Schmitt, K. Haug, "Measurements of the States of In Situ Stress for the Duvernay Formation near Fox Creek, West-Central Alberta," *AER/AGS Report* [https://ags.aer.ca/publications/REP\\_97.html](https://ags.aer.ca/publications/REP_97.html), (2018).
3. O. Heidbach, M. Rajabi, K. Reiter, M. Ziegler, WSM Team, Word Stress Map, Ed. (2016).
4. K. Haug, J. S. Bell. (Alberta Energy Regulator, AER/AGS Digital Data, 2016).
5. R. Schultz, R. Wang, Y. J. Gu, K. Haug, G. Atkinson, A seismological overview of the induced earthquakes in the Duvernay play near Fox Creek, Alberta. *Journal of Geophysical Research: Solid Earth* **122**, 492-505 (2017).
6. V. Vavryčuk, Iterative joint inversion for stress and fault orientations from focal mechanisms. *Geophysical Journal International* **199**, 69-77 (2014).
7. E. M. Anderson, *The dynamics of faulting and dyke formation with applications to Britain*. (Oliver and Boyd, 1942).
8. T. Terakawa, E. Hauksson, Absolute Stress Fields in the Source Region of the 1992 Landers Earthquake. *Journal of Geophysical Research: Solid Earth* **123**, 8874-8890 (2018).
9. A. Morris, D. A. Ferrill, D. B. Henderson, Slip-tendency analysis and fault reactivation. *Geology* **24**, 275-278 (1996).
10. D. R. Schmitt, C. A. Currie, L. Zhang, Crustal stress determination from boreholes and rock cores: Fundamental principles. *Tectonophysics* **580**, 1-26 (2012).

11. S. Chopra *et al.*, Seismic reservoir characterization of Duvernay shale with quantitative interpretation and induced seismicity considerations—A case study. *Interpretation* **5**, T185-T197 (2017).
12. R. Schultz *et al.*, Linking fossil reefs with earthquakes: Geologic insight to where induced seismicity occurs in Alberta. *Geophysical Research Letters* **43**, 2534-2542 (2016).
13. C. Marone, D. M. Saffer, Fault friction and the upper transition from seismic to aseismic faulting. *The Seismogenic Zone of Subduction Thrust Faults*, 346-369 (2007).
14. C. Marone, Laboratory-derived friction laws and their application to seismic faulting. *Annual Review of Earth and Planetary Sciences* **26**, 643-696 (1998).
15. J. H. Dieterich, Time-dependent friction in rocks. *Journal of Geophysical Research* **77**, 3690-3697 (1972).
16. J. H. Dieterich, in *Rock Friction and Earthquake Prediction*. (Springer, 1978), pp. 790-806.
17. E. Tenthorey, S. F. Cox, Cohesive strengthening of fault zones during the interseismic period: An experimental study. *Journal of Geophysical Research: Solid Earth* **111**, (2006).
18. J. Weiss, V. Pellissier, D. Marsan, L. Arnaud, F. Renard, Cohesion versus friction in controlling the long-term strength of a self-healing experimental fault. *Journal of Geophysical Research: Solid Earth* **121**, 8523-8547 (2016).
19. S. K. Muhuri, T. A. Dewers, T. E. Scott Jr, Z. e. Reches, Interseismic fault strengthening and earthquake-slip instability: Friction or cohesion? *Geology* **31**, 881-884 (2003).
20. R. W. Day, Effective cohesion for compacted clay. *Journal of geotechnical engineering* **118**, 611-619 (1992).
21. M. Scuderi, C. Collettini, C. Viti, E. Tinti, C. Marone, Evolution of shear fabric in granular fault gouge from stable sliding to stick slip and implications for fault slip mode. *Geology* **45**, 731-734 (2017).
22. M. J. Ikari, A. J. Kopf, Seismic potential of weak, near-surface faults revealed at plate tectonic slip rates. *Science advances* **3**, e1701269 (2017).
23. H. Sone, M. D. Zoback, Mechanical properties of shale-gas reservoir rocks—Part 2: Ductile creep, brittle strength, and their relation to the elastic modulus Mechanical properties of gas shale—Part 2. *Geophysics* **78**, D393-D402 (2013).
24. M. D. Zoback, *Reservoir geomechanics*. (Cambridge University Press, 2010).
25. W. L. Ellsworth, Injection-induced earthquakes. *Science* **341**, 1225942 (2013).
26. A. H. Kohli, M. D. Zoback, Frictional properties of shale reservoir rocks. *Journal of geophysical research: solid earth* **118**, 5109-5125 (2013).
27. M. Scuderi, C. Collettini, C. Marone, Frictional stability and earthquake triggering during fluid pressure stimulation of an experimental fault. *Earth and Planetary Science Letters* **477**, 84-96 (2017).
28. Y. Gu, T.-f. Wong, Development of shear localization in simulated quartz gouge: Effect of cumulative slip and gouge particle size. *pure and applied geophysics* **143**, 387-423 (1994).
29. B. Crawford, D. Faulkner, E. Rutter, Strength, porosity, and permeability development during hydrostatic and shear loading of synthetic quartz-clay fault gouge. *Journal of Geophysical Research: Solid Earth* **113**, (2008).

30. S. Tembe, D. A. Lockner, T. F. Wong, Effect of clay content and mineralogy on frictional sliding behavior of simulated gouges: Binary and ternary mixtures of quartz, illite, and montmorillonite. *Journal of Geophysical Research: Solid Earth* **115**, (2010).
31. M. Takahashi, K. Mizoguchi, K. Kitamura, K. Masuda, Effects of clay content on the frictional strength and fluid transport property of faults. *Journal of Geophysical Research: Solid Earth* **112**, (2007).
32. D. R. Scott, C. J. Marone, C. G. Sammis, The apparent friction of granular fault gouge in sheared layers. *Journal of Geophysical Research: Solid Earth* **99**, 7231-7246 (1994).
33. M. J. Ikari, C. Marone, D. M. Saffer, On the relation between fault strength and frictional stability. *Geology* **39**, 83-86 (2011).
34. M. J. Ikari, D. M. Saffer, C. Marone, Effect of hydration state on the frictional properties of montmorillonite-based fault gouge. *Journal of Geophysical Research: Solid Earth* **112**, (2007).
35. C. Morrow, D. E. Moore, D. Lockner, The effect of mineral bond strength and adsorbed water on fault gouge frictional strength. *Geophysical research letters* **27**, 815-818 (2000).
36. M. Nakatani, C. H. Scholz, Frictional healing of quartz gouge under hydrothermal conditions: 1. Experimental evidence for solution transfer healing mechanism. *Journal of Geophysical Research: Solid Earth* **109**, (2004).
37. C. Marone, C. B. Raleigh, C. Scholz, Frictional behavior and constitutive modeling of simulated fault gouge. *Journal of Geophysical Research: Solid Earth* **95**, 7007-7025 (1990).
38. J. M. Logan, K. A. Rauenzahn, Frictional dependence of gouge mixtures of quartz and montmorillonite on velocity, composition and fabric. *Tectonophysics* **144**, 87-108 (1987).
39. J. D. Weeks, T. E. Tullis, Frictional sliding of dolomite: A variation in constitutive behavior. *Journal of Geophysical Research: Solid Earth* **90**, 7821-7826 (1985).
40. J. Samuelson, C. J. Spiers, Fault friction and slip stability not affected by CO<sub>2</sub> storage: Evidence from short-term laboratory experiments on North Sea reservoir sandstones and caprocks. *Int. J. Greenh. Gas Control* **11**, S78-S90 (2012).
41. D. W. Eaton *et al.*, Induced Seismicity Characterization during Hydraulic Fracture Monitoring with a Shallow Wellbore Geophone Array and Broadband Sensors. *Seismological Research Letters* **89**, 1641-1651 (2018).